Submitted to the
International Conference on High Energy Physics
16-22 August 2004, Beijing, China

Abstract: 5-0344, 11-0345

Session: QCD hard interactions and Heavy quarks

Measurements of charm production in DIS

ZEUS Collaboration

Abstract

Charm production has been measured in deep inelastic scattering with the ZEUS detector at HERA using an integrated luminosity of about 80 pb^{-1}. The data compliment previous measurements by considering either different charm-tagging methods or a different range in the virtuality of the exchanged photon, Q^2. The data are compared with the predictions of next-to-leading-order QCD.

1 Introduction

Charm quarks in photoproduction and deep inelastic scattering (DIS) have been extensively studied at HERA [1–6]. These measurements are consistent with perturbative QCD calculations indicating boson-gluon fusion (BGF) as the dominant mechanism of charm production. For most of the charm DIS measurements only D^* mesons are selected and the Q^2 region is restricted to values above 1.5 GeV^2.

This paper presents the measurements of charm production in DIS using D^0, $D^\pm$, D_s and D^* mesons. The selection of D mesons other than D^* tests the effects of fragmentation and is an independent probe of the charm production mechanism. Measurements of the cross sections of the D mesons were performed in ep scattering at HERA in the DIS regime with $1.5 < Q^2 < 1000$ GeV^2. The results are compared to the predictions of next-to-leading-order (NLO) QCD calculations using the HVQDIS program [7].

Charm production in DIS at low Q^2 is also presented in this paper. By selecting D^* for $0.05 < Q^2 < 0.7$ GeV^2, the transition region from DIS to photoproduction is probed. This measurement was performed using the beam pipe calorimeter (BPC) [8, 9]. Differential cross sections have been measured as a function of Q^2, y, $p_T(D^*)$ and $\eta(D^*)$ and compared to NLO predictions using the HVQDIS program.

2 Experimental set-up

The data presented in this analysis were collected with the ZEUS detector at HERA during the 1998-2000 running periods, with $e^\pm$ beam energy of $E_e = 27.5$ GeV colliding with a proton beam energy of $E_p = 920$ GeV. The data sample corresponds to an integrated luminosity of 82 pb^{-1}.

A detailed description of the ZEUS detector can be found elsewhere [10]. A brief outline of the components that are most relevant for this analysis is given below.

Charged particles are tracked in the central tracking detector (CTD) [11], which operates in a magnetic field of 1.43 T provided by a thin superconducting solenoid. The CTD consists of 72 cylindrical drift chamber layers, organised in nine superlayers covering the polar-angle[1] region $15^\circ < \theta < 164^\circ$. The transverse-momentum resolution for full-length tracks is $\sigma(p_T)/p_T = 0.0058 p_T \oplus 0.0065 \oplus 0.0014/p_T$, with p_T in GeV.

[1] The ZEUS coordinate system is a right-handed Cartesian system, with the Z axis pointing in the proton beam direction, referred to as the "forward direction", and the X axis pointing left towards the centre of HERA. The coordinate origin is at the nominal interaction point.

The high-resolution uranium–scintillator calorimeter (CAL) [12] consists of three parts: the forward, the barrel and the rear calorimeters. The smallest subdivision of the calorimeter is called a cell. The CAL energy resolutions, as measured under test-beam conditions, are $\sigma(E)/E = 0.18/\sqrt{E}$ for electrons and $\sigma(E)/E = 0.35/\sqrt{E}$ for hadrons, with E in GeV.

The BPC is a small calorimeter designed to provide an accurate measurement of the energy and position of the electron at very small scattering angles. The detector covers the range $0.045 < Q^2 < 0.7$ GeV^2. There are 2 BPC modules installed – north and south. The north BPC is used for physics analysis and will be denoted as BPC. The south BPC module has a substantially reduced active area and is therefore used only for alignment and calibration. The BPC consists of 36 layers of 3.5 mm thick tungsten alloy absorber planes interleaved with 2.6 mm thick scintillator strips. It is about $24X_0$ along z ($\sim$ 16 cm). The energy resolution of the BPC is $\sigma(E)/E \sim 17\sqrt{E}$, with E in GeV.

3 D mesons

3.1 Event selection

An event was selected if it satisfied the following criteria: a scattered electron was identified using a neural-network procedure [13] with energy $E'_e > 10$ GeV; $y_e \leq 0.95$; $y_{JB} \geq 0.02$; $1.5 < Q^2_\Sigma < 1000$ GeV^2, where the subscripts e, JB and Σ stands for electron, Jaquet-Blondel [14] and Σ- [15] methods, respectively; $40 < \delta < 60$ GeV, where $\delta = \sum_i (E - p_z)_i$ and the index i runs over a combination of tracks measured in CTD and CAL clusters; a reconstructed primary vertex with $|Z_{\text{vertex}}| < 50$ cm is required; the impact point (X, Y) for the scattered lepton in the RCAL must lie outside the region 26×14 cm^2 centred on $X = Y = 0$.

The selected kinematic region was $1.5 < Q^2 < 1000$ GeV^2 and $0.02 < y < 0.7$.

3.2 Reconstruction of D mesons

The reconstruction of D^0, $D^\pm$, D_s and D^* mesons was performed in the kinematic region $p_T(D) > 3.0$ GeV and $|\eta(D)| < 1.6$. The distributions were fitted assuming a "modified" gaussian function, $\text{Gauss}^{\text{mod}} \propto \exp(-0.5\text{x}^{1+\frac{1}{1+0.5\text{x}}})$, where $x = |(M - M_D)/\sigma|$, to describe the signal shape plus a background function. Only tracks measured in the CTD fitted to a primary vertex were used in the reconstruction.

The D^0 mesons were reconstructed from the decay channel $D^0 \to K^-\pi^+$ (+c.c.). In each event, D^0 candidates are formed from pairs of tracks with opposite charges and

$p_T > 0.8$ GeV. A cut $|\cos(A)| < 0.8$, where $A = \text{angle}(\boldsymbol{p}_K^{(D^0\ \text{rest})}, \boldsymbol{p}_{D^0}^{(\text{lab})})$, was applied to reduce the contribution from combinatorial background. For D^0 mesons not coming from a D^*, the incorrect assignment of the pion and kaon masses to the two tracks produces a wider reflected signal. Figure 1 shows the $M(K\pi)$ distribution for D^0 candidates after the reflection subtraction. A clear signal is seen at the nominal value of $M(D^0)$. The number of D^0 mesons yielded by the fit was $N(D^0) = 10480 \pm 507$.

The $D^\pm$ mesons were reconstructed from the decay channel $D^\pm \to K^-\pi^+\pi^+$ (+c.c.). In each event, two tracks with the same charges and a third track with opposite charge are combined to form $D^\pm$ candidates. Each track is required to have $p_T > 0.8$ GeV. To reduce combinatorial background, a cut in the variable $\cos(A) > -0.6$ is imposed, where $A = \text{angle}(\boldsymbol{p}_K^{(D^\pm\ \text{rest})}, \boldsymbol{p}_{D^\pm}^{(\text{lab})})$. Figure 2 shows the $M(K\pi\pi)$ distributions for $D^\pm$ candidates. A clear signal is seen at the nominal value of $M(D^\pm)$. The number of $D^\pm$ mesons yielded by the fit was $N(D^\pm) = 2232 \pm 269$.

The D_s mesons were reconstructed from the decay channel $D_s^+ \to \phi\pi^+$ (+c.c.) with $\phi \to K^+K^-$. In each event, two tracks with opposite charges were combined to form the ϕ candidates satisfying the condition $1.011 < M(KK) < 1.027$ GeV. A third track is combined with the ϕ candidate yielding the D_s candidate. Only tracks with $p_T > 0.8$ GeV were considered. Combinatorial background can be supressed with the following cuts: $|\cos^3(B)| > 0.1$, where $B = \text{angle}(\boldsymbol{p}_K^{(\phi\ \text{rest})}, \boldsymbol{p}_\pi^{(\phi\ \text{rest})})$, and $\cos(A) < 0.85$, where $A = \text{angle}(\boldsymbol{p}_\pi^{(D_s\ \text{rest})}, \boldsymbol{p}_{D_s}^{(\text{lab})})$. Figure 3 shows the $M(KK\pi)$ distribution for D_s candidates. A clear signal is seen at the nominal value of $M(D_s)$. A secondary signal also appears at the nominal value of $M(D^\pm)$, as expected from the decay of $D^\pm$ in the same channel. The resulting mass distribution was fitted to the sum of two modified gaussians, one for each signal peak. The number of reconstructed D_s mesons yielded by the fit was $N(D_s) = 578 \pm 74$.

The D^* mesons were reconstructed from the decay channels $D^{*+} \to D^0\pi_s^+$ (+c.c.) with $D^0 \to K^-\pi^+$ (+c.c.). In each event, pairs of tracks with $p_T > 0.4$ GeV were combined to form a D^0 candidate. Only combinations with invariant mass $1.80 < M(K\pi) < 1.92$ GeV were considered. A third track with $p_T > 0.12$ GeV and charge opposite to that of the kaon track was combined with the D^0 candidate to form a D^* candidate, and kept if its charge was opposite to the kaon track. Figure 4 shows the distribution of the mass difference $\Delta M = M(K\pi\pi_s) - M(K\pi)$ for D^* candidates. A clear signal is seen around the nominal value of $M(D^*) - M(D^0)$. The number of reconstructed D^* mesons was obtained from the wrong-charge subtraction method and from the fit of ΔM distribution. The combinatorial background under the signal was estimated from the mass difference distribution of the wrong-charge combinations, in which both tracks associated to the D^0 candidate have the same charge and the third track has opposite charge. The number of reconstructed D^* mesons was calculated by subtracting the wrong charge ΔM distribution, after normalizing it to the number of right charge candidates in the region $0.150 < \Delta M < 0.165$ GeV. The subtraction was done in the signal region $0.143 < \Delta M < 0.148$ GeV, and yielded $N(D^*) = 3187 \pm 74$, whereas the fit of the ΔM distribution yielded $N(D^*) = 3258 \pm 77$.

3.3 Cross sections

The inclusive charm mesons cross sections were measured in the kinematic region $1.5 < Q^2 < 1000$ GeV^2, $0.02 < y < 0.7$, $p_T(D) > 3.0$ GeV and $|\eta| < 1.6$. The RAPGAP [16] Monte Carlo program was used to correct the data for detector effects and calculate acceptances. The measured cross sections are:

$$\begin{aligned}
\sigma(e^{\pm}p \to e^{\pm}D^0X) &= 7.44 \pm 0.78(\mathrm{stat})^{+0.29}_{-0.49}(\mathrm{syst})\ \mathrm{nb};\\
\sigma(e^{+}p \to e^{+}D^{\pm}X) &= 2.42 \pm 0.30(\mathrm{stat})^{+0.21}_{-0.06}(\mathrm{syst})\ \mathrm{nb};\\
\sigma(e^{\pm}p \to e^{\pm}D_sX) &= 2.25 \pm 0.30(\mathrm{stat})^{+0.09}_{-0.33}(\mathrm{syst})\ \mathrm{nb};\\
\sigma(e^{\pm}p \to e^{\pm}D^*X) &= 3.22 \pm 0.08(\mathrm{stat})^{+0.07}_{-0.05}(\mathrm{syst})\ \mathrm{nb}
\end{aligned}$$

The D^* cross section obtained from wrong-charge background subtraction agrees very well with the one obtained from the fit. The main sources of systematic errors came from the use of double angle [17, 18] method to reconstruct the kinematic variables for the D^0 and D^* mesons, lowering the cut on the p_T of the tracks to 0.7 GeV for the D_s meson, and increasing the cut on the p_T of the tracks to 0.9 GeV for the $D^{\pm}$ meson.

3.4 NLO QCD predictions

The NLO prediction of the $c\bar{c}$ cross section was obtained using the program HVQDIS. The fragmentation of the charm quarks was performed according to the Peterson model with the parameter $\epsilon = 0.035$. The nominal mass of the charm quark was set to $m_c = 1.35$ GeV. The normalisation and factorisation scales were set to $\mu = \sqrt{Q^2 + 4m_c^2}$. The fragmentation fractions $f(c \to D)$ were taken from combined e^+e^- measurements [19]. The recent ZEUS NLO QCD global fit [20] was used as the parametrisation of the proton

PDFs. The NLO predictions are:

$$\sigma_{HVQDIS}(e^{\pm}p \rightarrow e^{\pm}D^{0}X) = 7.14 \text{ nb}$$
$$\sigma_{HVQDIS}(e^{\pm}p \rightarrow e^{\pm}D^{\pm}X) = 3.02 \text{ nb}$$
$$\sigma_{HVQDIS}(e^{\pm}p \rightarrow e^{\pm}D_{s}X) = 1.32 \text{ nb}$$
$$\sigma_{HVQDIS}(e^{\pm}p \rightarrow e^{\pm}D^{*}X) = 3.06 \text{ nb}$$

The measured D^* and D^0 cross sections agree with the predictions based on NLO and fragmentation fractions from e^+e^-, however 20% of the D^0 come from D^*. The $D^\pm$ and D_s cross sections deviate 18% and 71%, respectively, from the predictions.

4 D^* production at low Q^2

4.1 Event selection

Events which fulfil the following conditions are selected: characteristic energy deposite of an electron within the fiducial area of the BPC with $E_{BPC} > 4$ GeV; BPC timing measurement consistent with an ep interaction $| < \tau_{BPC} > | < 3$ ms; a primary vertex with $|Z_{vertex} < 50|$ cm is reconstructed; the ratio of the transverse momentum of the D^* to the total tranverse CAL energy deposit is $p_t(D*)/E_t > 0.1$ and $35 < \delta_{BPC} < 65$ GeV, where $\delta_{BPC} = \delta + E_{BPC}(1 - \cos(\Theta_{BPC}))$, $\delta = \sum_i (E - p_z)_i$, and the index i runs over the CAL clusters and Θ_{BPC} is the angle of the scattered electron w.r.t. the proton beam axis. Events with an additional reconstructed electron in the calorimeter are suppressed.

The selected kinematic region was $0.05 < Q^2 < 0.7$ GeV^2 and $0.02 < y < 0.85$.

4.2 Reconstruction of D^* mesons

The D^* mesons were reconstructed from the decay channels $D^{*+} \rightarrow D^0\pi_s^+$ (+c.c.) with $D^0 \rightarrow K^-\pi^+$ (+c.c.). The procedure to combine tracks to form D^0 and D^* candidates is the same as that described above. The tracks associated to D^0 must have $p_T > 0.45$ GeV and those associated to the π_s, $p_T > 0.12$ GeV. A different mass window for D^0 was used for each bin of $p_T(D^*)$: $1.82 < M(K\pi) < 1.91$ GeV, $1.81 < M(K\pi) < 1.92$ GeV, $1.80 < M(K\pi) < 1.93$ GeV and $1.79 < M(K\pi) < 1.94$ GeV for $1.5 < p_T(D^*) < 3.25$ GeV, $3.25 < p_T(D^*) < 5$ GeV, $5 < p_T(D^*) < 8$ GeV and $8 < p_T(D^*) < 9$ GeV, respectively.

D^* mesons were selected in the kinematic region $1.5 < p_T(D^*) < 9$ GeV and $|\eta(D^*)| < 1.5$.

Figure 5 shows the ΔM distribution measured using BPC. The number of D^* mesons, extracted by an unbinned fit, was $N(D^*) = 253 \pm 25$.

4.3 Cross sections

The inclusive D^* cross sections at low Q^2 were measured in the kinematic region $0.05 < Q^2 < 0.7$ GeV^2, $0.02 < y < 0.85$, $1.5 < p_T(D^*) < 9$ GeV, $|\eta(D^*)| < 1.5$. The HERWIG [21] Monte Carlo program was used to correct the data for detector effects and calculate acceptances. The measured cross section is

$$\sigma(e^{\pm}p \to e^{\pm}D^*X) = 10.1 \pm 1.0(\text{stat})^{+1.1}_{-0.8}(\text{syst})\ \text{nb}.$$

The replacement of HERWIG by RAPGAP for acceptance corrections was the main source of systematic error.

Figures 6-9 show the single differential cross sections as a function of Q^2, y, $p_T(D^*)$ and $\eta(D^*)$ compared to the NLO QCD predictions. In general, shape and normalization of the distributions are described by the NLO predictions. A comparison of $d\sigma/dQ^2$ with previous ZEUS results is shown in figure 10. For this figure, in order to have data comparable to older measurements, the y range was restricted to $0.02 < y < 0.7$. The unbinned fit in this restricted kinematic region yields $N(D^*) = 239 \pm 23$.

4.4 NLO QCD predictions

The NLO prediction of the $c\bar{c}$ cross section was obtained using the program HVQDIS. At low Q^2, HVQDIS is applicable because the calculation neglects terms of orders higher than α_s^2. These terms contain $\log(Q^2/m_c^2)$ factors which can become large for $Q^2 \gg m_c^2$. Therefore, the HVQDIS results are expected to be more accurate at $Q^2 \approx m_c^2$. The fragmentation of the charm quarks was performed according to the Peterson model with the parameter $\epsilon = 0.035$. The nominal mass of the charm quark was set to $m_c = 1.35$ GeV. The normalisation and factorisation scales were set to $\mu = \sqrt{Q^2 + 4m_c^2}$. The ZEUS NLO QCD fit and CTEQ5F3 were used as the parametrisation of the proton PDFs. The NLO predicted total cross section is

$$\sigma_{HVQDIS}(e^{\pm}p \to e^{\pm}D^*X) = 8.6^{+1.9}_{-1.8}(\text{syst.})\,\text{nb}$$

To estimate the theoretical uncertainty, the ZEUS PDF fit [20] was used and the scale μ, the mass of the charm quark and the parameter ϵ in the Peterson fragmentation function were varied in the range: $(Q^2 + m_c^2) < \mu^2 < 4(Q^2 + 4m_c^2)$, $1.2 < m_c < 1.5$ GeV, $0.02 < \epsilon < 0.05$, respectively. The mass variation is the dominant source of uncertainty.

5 Summary

The production of D^0, $D^{\pm}$, $D_s^{\pm}$ and $D^{*\pm}$ charm mesons has been measured in DIS at HERA in the kinematic region $1.5 < Q^2 < 1000$ GeV^2, $0.02 < y < 0.7$, $p_T(D) > 3.0$ GeV and $|\eta| < 1.6$ with the ZEUS detector. The measured D^0 and D^* cross sections agree with the predictions based on NLO and fragmentation fractions from e^+e^- measurements. The measured $D^{\pm}$ and $D_s^{\pm}$ cross sections have some deviations from the predictions.

The production of D^* mesons in DIS at HERA was measured with the ZEUS detector in the kinematic region $0.05 < Q^2 < 0.7$ GeV^2, $0.02 < y < 0.85$, $1.5 < p_T(D^*) < 9$ GeV, $|\eta(D^*)| < 1.5$, probing the transition region to photoproduction regime. The theoretical NLO QCD calculation of BGF charm production is consistent with the measured cross sections at low Q^2.

References

[1] ZEUS Coll., S. Chekanov et al., Phys. Rev. **D 69**, 0120004 (2004).

[2] H1 Coll., C. Adloff et al., Phys. Lett. **B 528**, 199 (2002).

[3] ZEUS Coll., J. Breitweg et al., Phys. Lett. **B 481**, 213 (2000).

[4] ZEUS Coll., J. Breitweg et al., Eur. Phys. J. **C 12**, 35 (2000).

[5] H1 Coll., C. Adloff et al., Nucl. Phys. **B 545**, 21 (1999).

[6] ZEUS Coll., J. Breitweg et al., Eur. Phys. J. **C 6**, 67 (1999).

[7] B. W. Harris and J. Smith, PR **D**, 2806 (1998).

[8] C. Amelung, *Measurement of the Proton Structure Function F_2 at Very Low Q^2 at HERA*. Ph.D. Thesis, Universität Bonn, Bonn, (Germany), Report BONN-IR-99-14, DESY-THESIS-2000-002, 1999.

[9] B. Surrow, *Measurement of the proton structure function F_2 at low Q^2 and very low x with the ZEUS beam pipe calorimeter at HERA*. Ph.D. Thesis, Hamburg University, Report DESY-THESIS-1998-004, 1998.

[10] ZEUS Coll., U. Holm (ed.), *The ZEUS Detector*. Status Report (unpublished), DESY (1993), available on `http://www-zeus.desy.de/bluebook/bluebook.html`.

[11] N. Harnew et al., Nucl. Inst. Meth. **A 279**, 290 (1989);
B. Foster et al., Nucl. Phys. Proc. Suppl. **B 32**, 181 (1993);
B. Foster et al., Nucl. Inst. Meth. **A 338**, 254 (1994).

[12] M. Derrick et al., Nucl. Inst. Meth. **A 309**, 77 (1991);
A. Andresen et al., Nucl. Inst. Meth. **A 309**, 101 (1991);
A. Caldwell et al., Nucl. Inst. Meth. **A 321**, 356 (1992);
A. Bernstein et al., Nucl. Inst. Meth. **A 336**, 23 (1993).

[13] H. Abramowicz, A. Caldwell and R. Sinkus, Nucl. Inst. Meth. **A 365**, 508 (1995).

[14] F. Jacquet and A. Blondel, *Proceedings of the Study for an ep Facility for Europe*, U. Amaldi (ed.), p. 391. Hamburg, Germany (1979). Also in preprint DESY 79/48.

[15] U. Bassler and G. Bernardi, Nucl. Inst. Meth. **A 361**, 197 (1995).

[16] H. Jung, Comp. Phys. Comm. **86**, 147 (1995).

[17] S. Bentvelsen, J. Engelen and P. Kooijman, *Proc. Workshop on Physics at HERA*, W. Buchmüller and G. Ingelman (eds.), Vol. 1, p. 23. Hamburg, Germany, DESY (1992).

[18] K.C. Höger, *Proc. Workshop on Physics at HERA*, W. Buchmüller and G. Ingelman (eds.), Vol. 1, p. 43. Hamburg, Germany, DESY (1992).

[19] L. Gladilin, Preprint hep-ex/9912064, 1999.

[20] ZEUS Coll., S. Chekanov et al., Phys. Rev. **D 67**, 012007 (2003).

[21] G. Marchesini et al., Comp. Phys. Comm. **67**, 465 (1992).

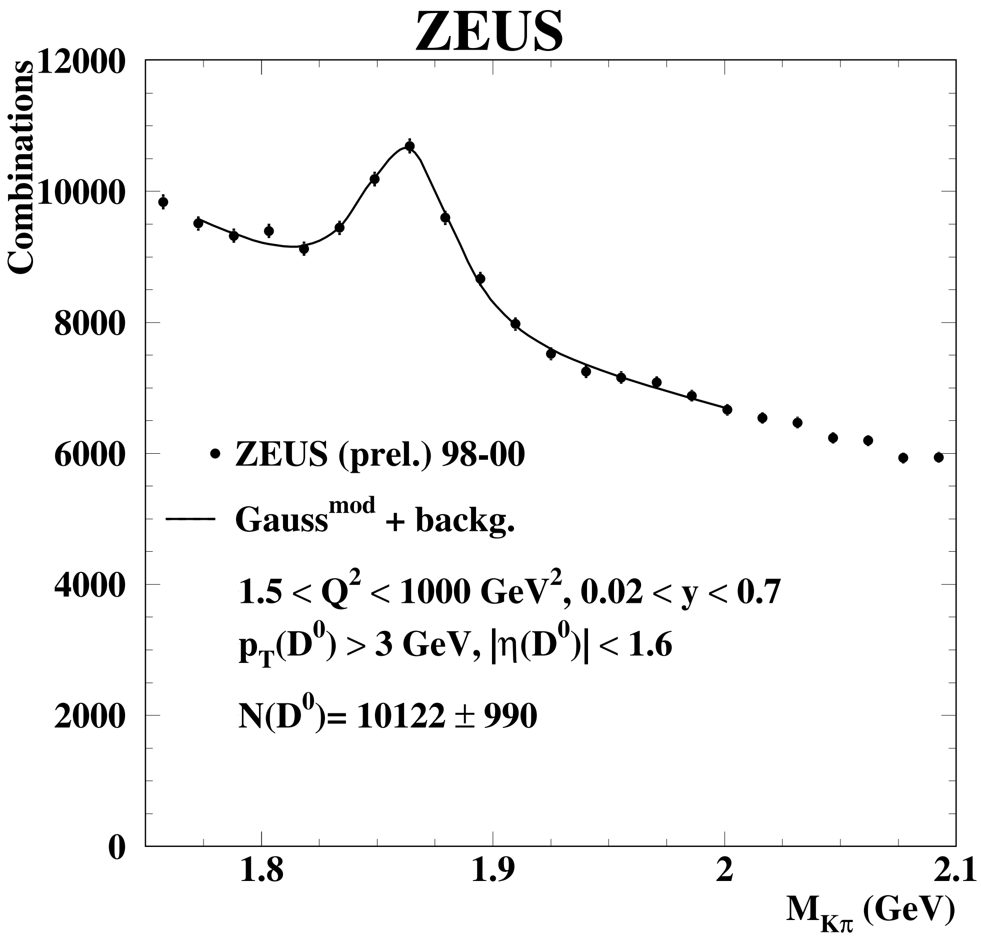

Figure 1: *The $M(K\pi)$ distribution for the D^0 candidates. The solid curve represents a fit to the sum of a modified Gaussian function and a background function.*

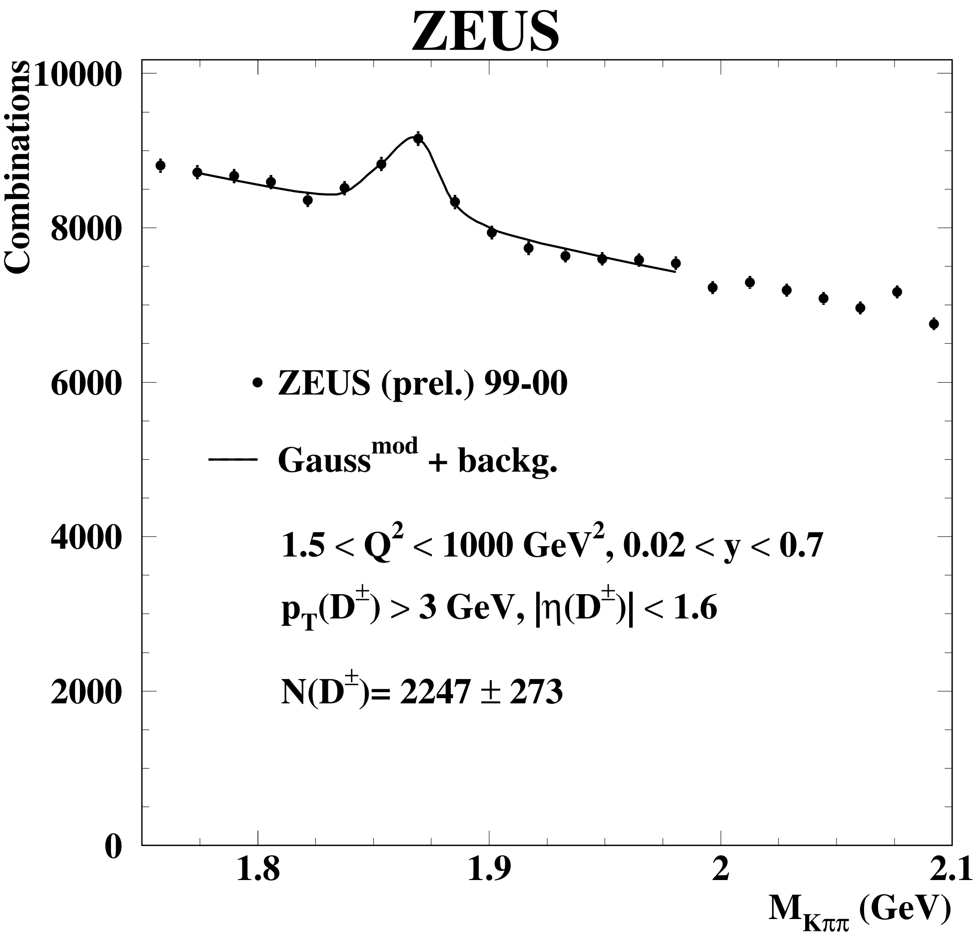

Figure 2: *The $M(K\pi\pi)$ distribution for the $D^\pm$ candidates. The solid curve represents a fit to the sum of a modified Gaussian function and a background function.*

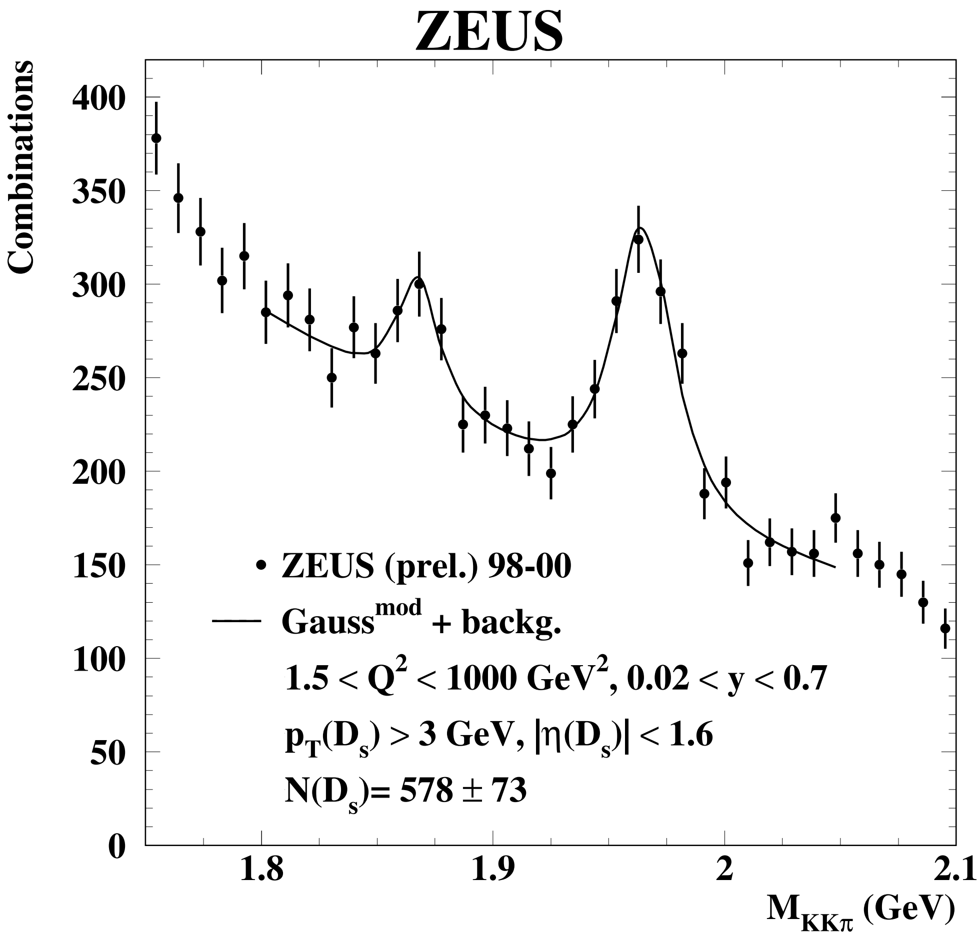

Figure 3: *The $M(KK\pi)$ distribution for the D_s candidates. The solid curve represents a fit to the sum of a modified Gaussian function and a background function.*

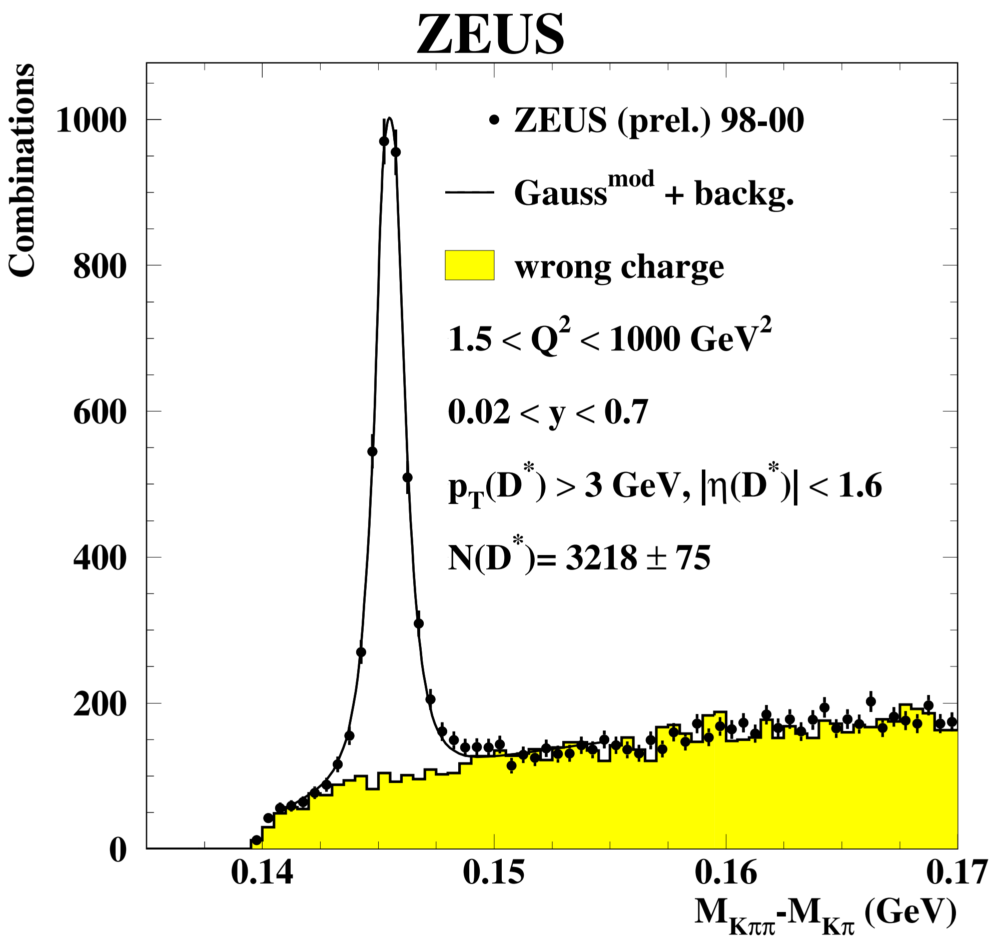

Figure 4: *The distribution of the mass difference, $\Delta M = M(K\pi\pi_s) - M(K\pi)$, for $D^{*\pm}$ candidates. The histogram shows the ΔM distribution for wrong charge combinations. The solid curve represents a fit to the sum of a modified Gaussian function and a background function.*

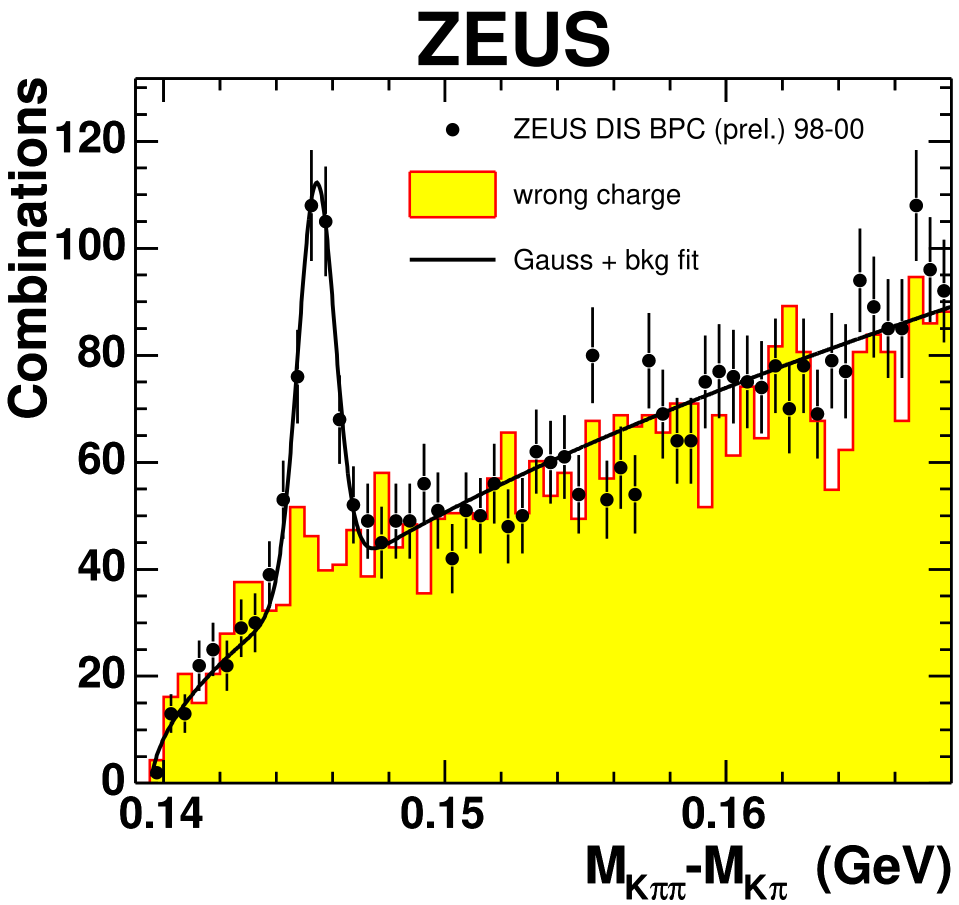

Figure 5: *The distribution of the mass difference, $\Delta M = M(K\pi\pi_s) - M(K\pi)$, for $D^{*\pm}$ candidates from BPC measurements. The histogram shows the ΔM distribution for wrong charge combinations. The solid curve represents the fit.*

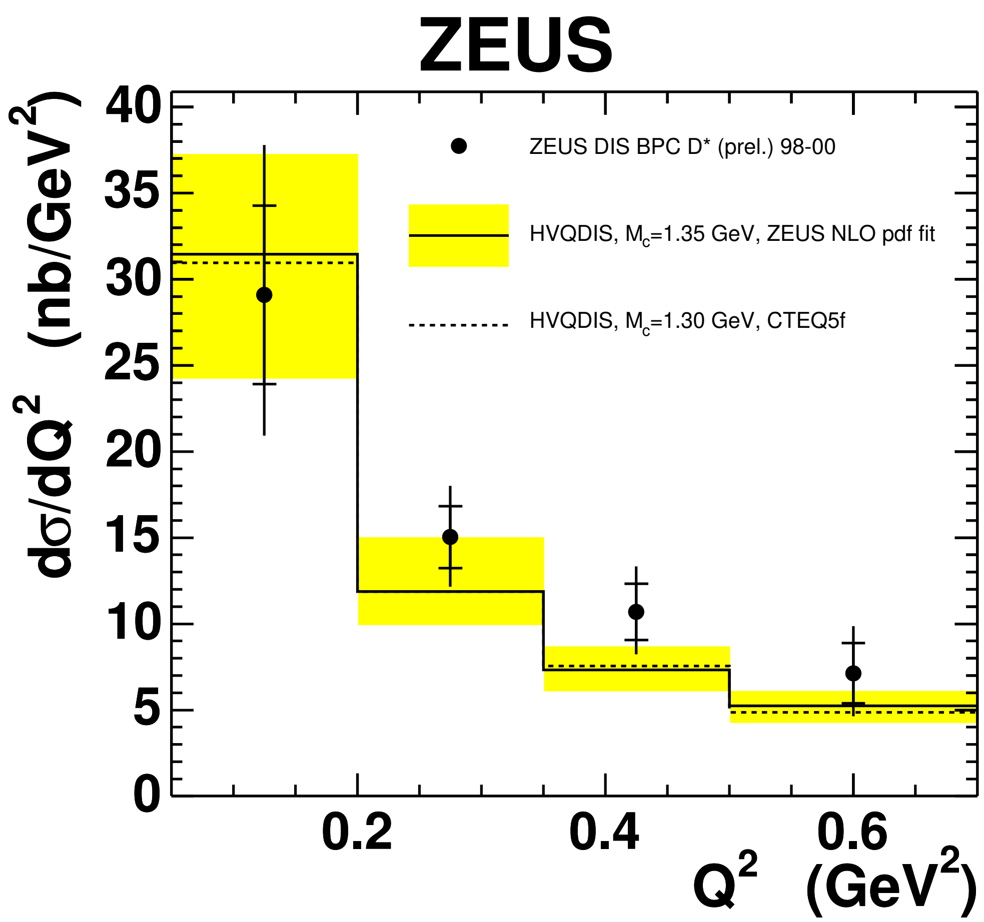

Figure 6: *Differential D^* cross sections as a function of Q^2 compared to the NLO predictions of HVQDIS.*

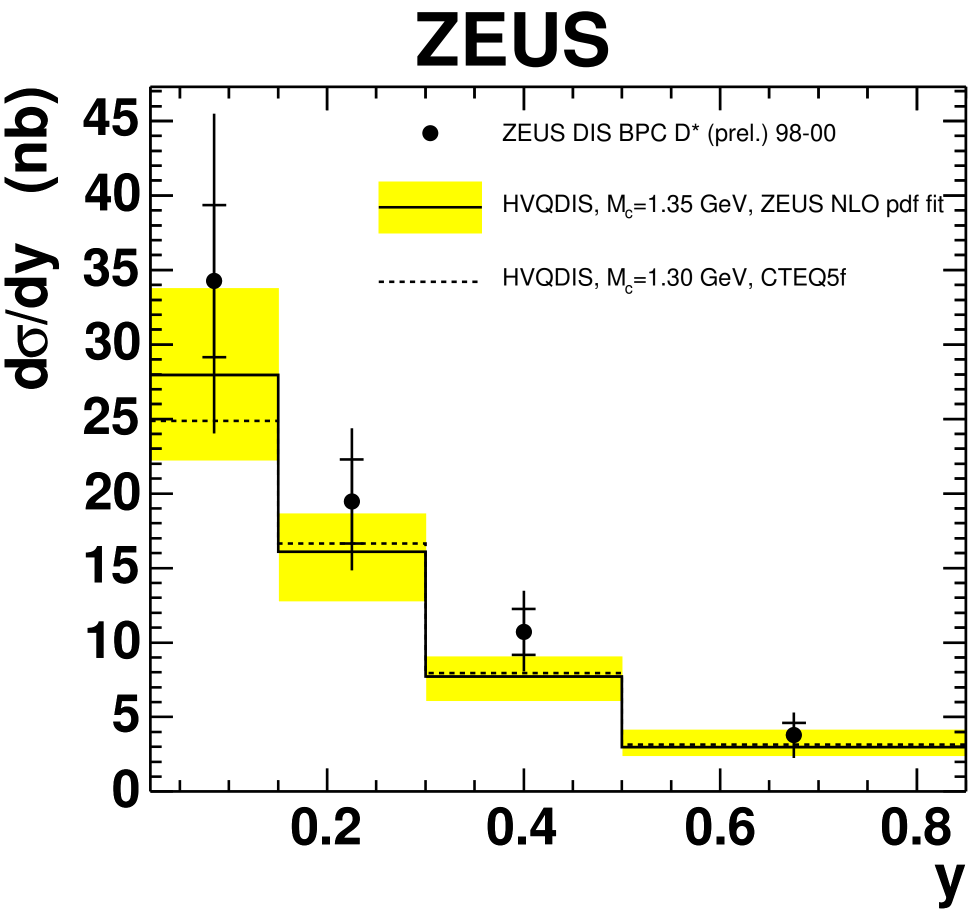

Figure 7: *Differential D^* cross sections as a function of y compared to the NLO predictions of HVQDIS.*

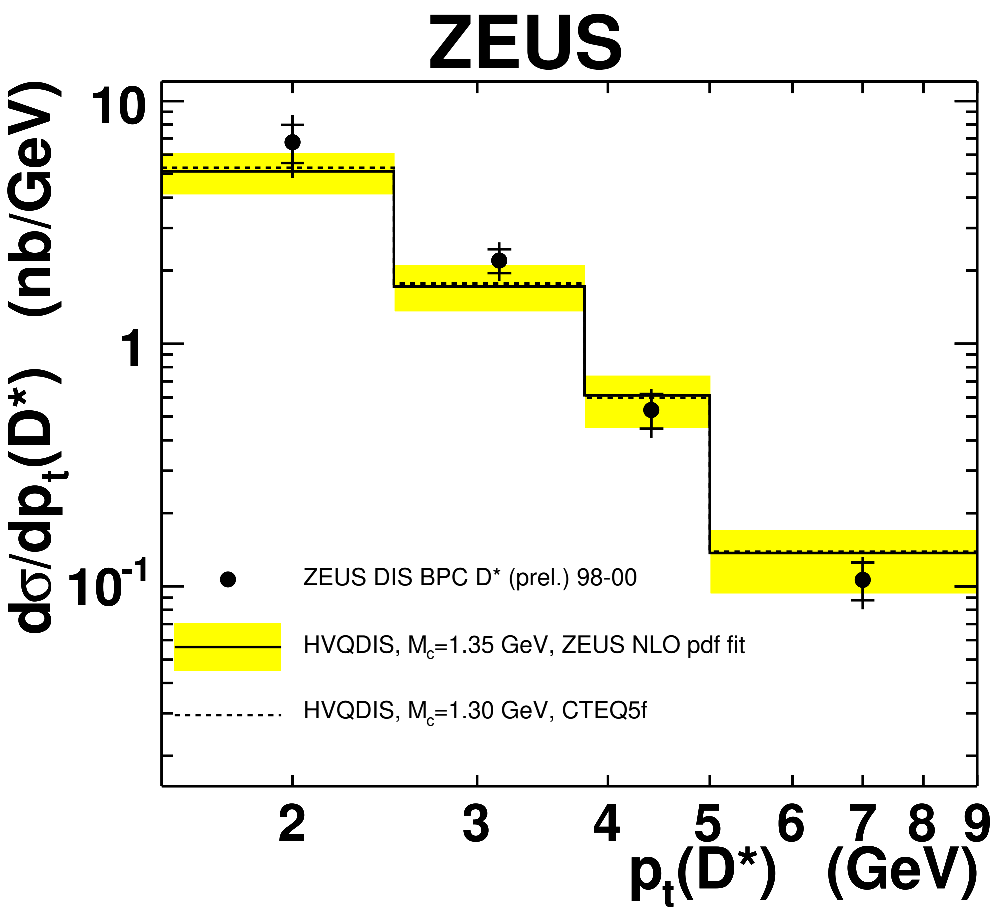

Figure 8: *Differential D^* cross sections as a function of $p_T(D^*)$ compared to the NLO predictions of HVQDIS.*

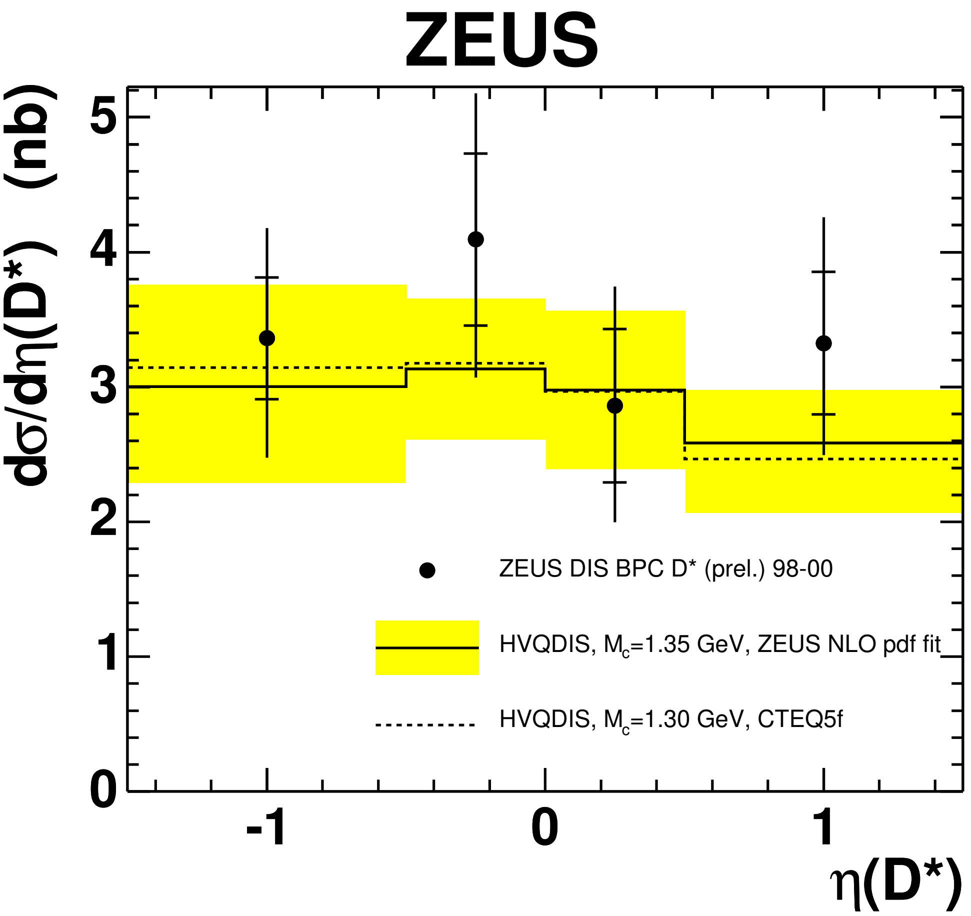

Figure 9: *Differential D^* cross sections as a function of $\eta(D^*)$ compared to the NLO predictions of HVQDIS.*

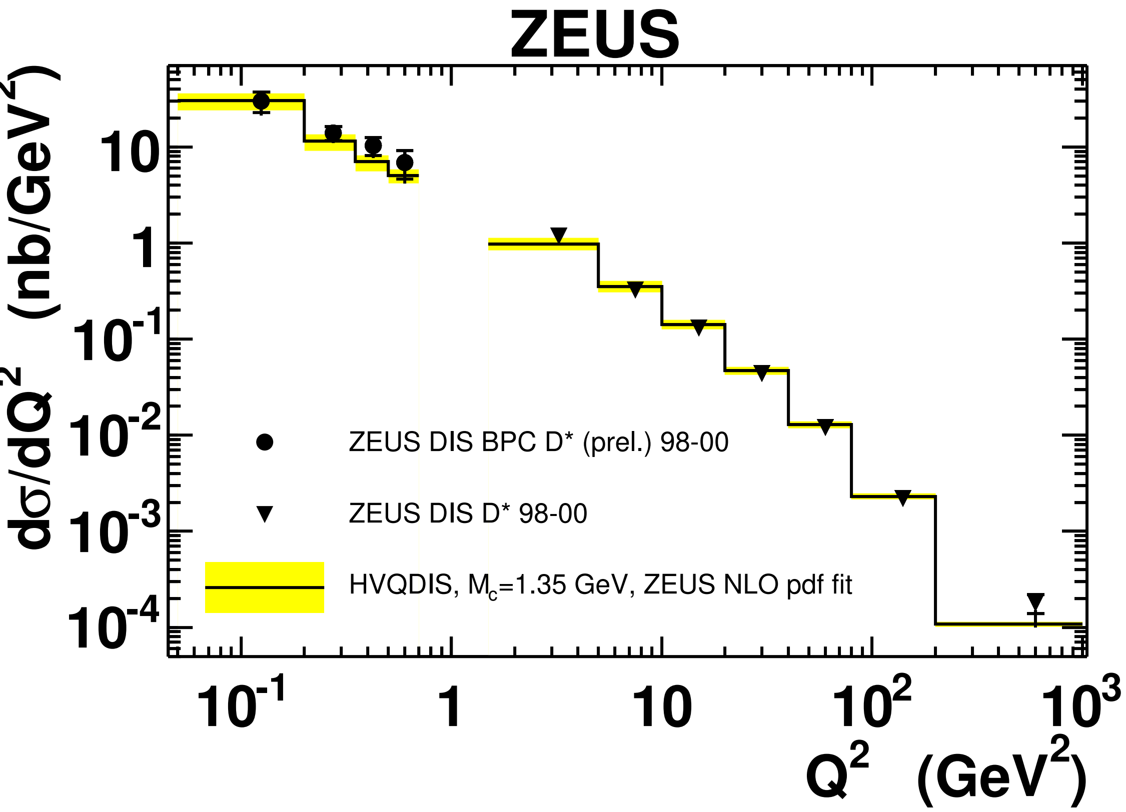

Figure 10: *Differential D^* cross sections as a function of Q^2 for low Q^2 and from previous results on D^* production in DIS compared to the NLO predictions from HVQDIS.*